

Microscopic calculation of ^{240}Pu scission with a finite-range effective force

W. Younes, and D. Gogny

Lawrence Livermore National Laboratory, Livermore, CA 94551

(Dated: November 25, 2018)

Abstract

Hartree-Fock-Bogoliubov calculations of hot fission in ^{240}Pu have been performed with a newly-implemented code that uses the D1S finite-range effective interaction. The hot-scission line is identified in the quadrupole-octupole-moment coordinate space. Fission-fragment shapes are extracted from the calculations. A benchmark calculation for ^{226}Th is obtained and compared to results in the literature. In addition, technical aspects of the use of HFB calculations for fission studies are examined in detail. In particular, the identification of scission configurations, the sensitivity of near-scission calculations to the choice of collective coordinates in the HFB iterations, and the formalism for the adjustment of collective-variable constraints are discussed. The power of the constraint-adjustment algorithm is illustrated with calculations near the critical scission configurations with up to seven simultaneous constraints.

I. INTRODUCTION

The last three decades have seen a resurgence of interest in the microscopic description of nuclear fission. This renaissance in fission theory has been ushered in by progress in formal many-body theory and by the advent of faster and parallel computers. The microscopic approach can boast a well-established track record of accomplishment over the last three decades, such as the prediction of fission barriers [1, 2, 3, 4, 5, 6, 7], and their evolution with temperature [8] and angular momentum [9], the prediction of fission times [2, 10] and fission-isomer lifetimes [11], the description of hot and cold fission [2], the prediction of fission yields [12], the description of cluster radioactivity as very asymmetric fission [13], and most recently, the calculation of fission-fragment properties (e.g., excitation energy, shape, kinetic energy, emitted-neutron multiplicity, angular momentum) [14, 15]. Despite these successes however, the microscopic description of fission remains one of the most difficult challenges in nuclear physics.

On the other hand, the promise of a microscopic theory that can reliably predict nearly all aspects of fission within a single, self-consistent framework is tantalizing. A fully self-consistent, dynamical approach to fission has been developed by the group at Bruyères-le-Châtel [2, 12, 14], and is being implemented at Livermore [16]. This approach treats both static and dynamic aspects of fission self-consistently and requires as its only phenomenological input the effective interaction between the nucleons.

A Hartree-Fock-Bogoliubov (HFB) code is the central tool for the description of the static aspects of fission in the microscopic method. The use of a finite-range effective interaction, such as the D1S interaction [17], allows for the treatment of pairing within the HFB formalism [18] in a fully self-consistent manner, and without the need for additional phenomenological parameters. The HFB calculations can be constrained by a judicious choice of collective variables to explore those nuclear shapes that are relevant to fission. Such constraints have confirmed the richness of fission phenomena, for example by revealing the full range of fission modes from hot (fragments formed in maximally-excited states) to cold (fragments formed with no excitation energy) [2].

In the dynamical component of the microscopic theory, a wave packet is built from HFB solutions constrained over all relevant nuclear shapes using the Time-Dependent Generator-Coordinate Method (TDGCM) [19, 20, 21, 22]. In practical applications, the

Gaussian-Overlap Approximation (GOA) to the TDGCM can be used to produce a collective Schrödinger equation, and therefore a collective Hamiltonian, constructed entirely from the single-particle degrees of freedom. The TDGCM formalism describes the nucleus in its lowest-energy state, as well as its collective excitations [23, 24], and can be extended to include intrinsic excitations as well [25] on the way to scission. These intrinsic excitations are needed for a microscopic description of fission that goes beyond the standard adiabatic approximation usually adopted in fission calculations [26]. This comprehensive program for the microscopic description of induced fission has already shown the importance of dynamical effects in the prediction of fission times [2] and fission-fragment yields [12], but a great deal of work remains to include all the relevant physics aspects in the calculation. In particular, a detailed and quantitative understanding of scission itself remains to be developed even at the level of the static calculations.

In this paper, we focus on the static aspect of the microscopic theory with three goals in mind: 1) to introduce the newly-developed HFB code FRANCHBRIE [16], which uses a finite-range effective interaction, 2) to examine in detail some basic technical aspects of fission calculations with an HFB code, and 3) to present first-time results of scission properties for the hot fission of ^{240}Pu . In section II we review the HFB formalism and discuss in detail some features of the one-center deformed harmonic-oscillator basis, formal and practical aspects of HFB fission calculations with multiple constraints, as well as the HFB convergence algorithm itself. In section III, we benchmark our HFB code against two-center calculations of scission properties for ^{226}Th by Dubray *et al.* [14]. We then apply the code to the identification of hot-scission configurations in ^{240}Pu , and the shapes of the nascent fragments just before scission.

II. THEORY

A. General HFB formalism

For convenience, we recall the main points of the HFB formalism with a finite-range effective interaction in this section and refer the reader to the literature for further details (see, e.g., [27, 28, 29]). We have implemented this formalism within the code FRANCHBRIE [16].

We start from the many-body Hamiltonian in second-quantized notation (see, e.g., chapter 5 in [27]),

$$H = \sum_{mn} t_{mn} a_m^\dagger a_n + \frac{1}{4} \sum_{mnpq} \bar{\mathcal{V}}_{mnpq} a_m^\dagger a_n^\dagger a_q a_p$$

with the antisymmetrized two-body matrix elements

$$\bar{\mathcal{V}}_{mnpq} \equiv \langle mn | \mathcal{V} | pq \rangle - \langle mn | \mathcal{V} | qp \rangle$$

and the usual anticommutation rules for particle operators

$$\{a_m, a_n\} = \{a_m^\dagger, a_n^\dagger\} = 0, \quad \{a_m^\dagger, a_n\} = \delta_{mn} \quad (1)$$

In this paper, we use a finite-range effective interaction which in coordinate space takes the form [28]

$$\begin{aligned} & \mathcal{V}(\vec{r}_1, \vec{r}_2) \\ &= \sum_{i=1}^2 \left(W_i + B_i \hat{P}_\sigma - H_i \hat{P}_\tau - M_i \hat{P}_\sigma \hat{P}_\tau \right) e^{-(\vec{r}_1 - \vec{r}_2)^2 / \mu_i^2} \\ & \quad + i W_{LS} \overleftarrow{\nabla}_{12} \times \delta(\vec{r}_1 - \vec{r}_2) \overrightarrow{\nabla}_{12} \cdot (\vec{\sigma}_1 + \vec{\sigma}_2) \\ & \quad + t_0 \left(1 + x_0 \hat{P}_\sigma \right) \delta(\vec{r}_1 - \vec{r}_2) \rho^\gamma \left(\frac{\vec{r}_1 + \vec{r}_2}{2} \right) + V_{\text{Coul}} \end{aligned} \quad (2)$$

where $\overleftarrow{\nabla}_{12} \equiv \overleftarrow{\nabla}_1 - \overleftarrow{\nabla}_2$, $\overrightarrow{\nabla}_{12} \equiv \overrightarrow{\nabla}_1 - \overrightarrow{\nabla}_2$, \hat{P}_σ is the spin-exchange operator, and \hat{P}_τ is the isospin-exchange operator. The Coulomb interaction V_{Coul} is added if both particles are protons, and $\rho(\vec{r})$ denotes the total nuclear density. The D1S effective interaction [2, 4] has been used for the present calculations. Given the computationally-intensive nature of the calculations, we have omitted contributions from the spin-orbit and Coulomb interactions to the pairing field. This approximation is well justified in the case of the spin-orbit interaction whose intensity in the singlet-even channel is very weak, but less so for the Coulomb term that can significantly reduce the pairing correlations for proton pairs [30]. We note also that the density-dependent part of the interaction is adjusted to cancel in the singlet-even channel by setting $x_0 = 1$. Consequently, only the Gaussian terms contribute to the pairing field, which permits the fully self-consistent application of the Bogoliubov formalism, without the need for arbitrary truncations of the space or the use of ad-hoc pairing forces. The Coulomb exchange contribution has been treated in the Slater approximation, and the two-body contribution to the center-of-mass correction has been included in the mean field.

The Bogoliubov theory [18] takes into account, in an approximate way, two-body correlations beyond the mean-field restriction to particle-hole excitations. The approach defines quasiparticle creation and destruction operators as linear combinations of the particle creation and destruction operators,

$$\begin{aligned}\eta_{\mu}^{\dagger} &\equiv \sum_n (U_{n\mu} a_n^{\dagger} + V_{n\mu} a_n) \\ \eta_{\mu} &\equiv \sum_n (U_{n\mu}^* a_n + V_{n\mu}^* a_n^{\dagger})\end{aligned}\quad (3)$$

Assuming there exists a vacuum of the destruction operators η_{μ} , denoted by $|\tilde{0}\rangle$, we identify it as the ground state of the nucleus and its energy can be written simply as a functional of the density matrix and the pairing tensor or, equivalently, as a functional of the generalized density

$$R \equiv \begin{pmatrix} \rho & -\kappa \\ \kappa^* & I - \rho^* \end{pmatrix} \equiv \begin{pmatrix} R^{11} & R^{12} \\ R^{21} & R^{22} \end{pmatrix}\quad (4)$$

We recall that the unitarity condition of the transformation in Eq. (3) is equivalent to

$$R^2 = R\quad (5)$$

we will therefore write the energy as

$$\begin{aligned}E(\rho, \kappa, \lambda_p, \lambda_n, \Lambda) \\ = E(\rho, \kappa) - \lambda_p \langle \tilde{0} | \hat{N}_p | \tilde{0} \rangle - \lambda_n \langle \tilde{0} | \hat{N}_n | \tilde{0} \rangle \\ - \text{Tr} [\Lambda (R^2 - R)]\end{aligned}\quad (6)$$

where $E(\rho, \kappa)$ is the expectation value of the Hamiltonian in the quasiparticle ground state, λ_p and λ_n are the Lagrange parameters needed to impose the appropriate average number of protons and neutrons, respectively, given by the matrix R . The matrix Λ of Lagrange parameters is needed to satisfy Eq. (5). Thus the determination of the fundamental nuclear state amounts to finding the generalized density matrix that minimizes Eq. (6). Some authors recognize Eq. (6) as the equation of a multidimensional surface, and seek its minimum directly using standard mathematical techniques to find the minimum of a function. Among these approaches, we cite the gradient method [31] or an improved variant known as the conjugate gradient method [32]. The number and diversity of applications using this method

speak to its effectiveness [7, 8, 9, 13, 33, 34]. In our approach to the minimization of Eq. (6), we start with the variational principle,

$$\begin{aligned}\delta E(\rho, \kappa, \lambda_p, \lambda_n, \Lambda) &= \text{Tr} \{ [\mathcal{H} - (\Lambda R + R\Lambda - \Lambda)] \delta R \} \\ &= 0\end{aligned}\tag{7}$$

$\forall \delta R$ where

$$\mathcal{H}_{mn}^{ij} \equiv 2 \frac{\delta E(\rho, \kappa, \lambda_p, \lambda_n)}{\delta R_{nm}^{ji}}\tag{8}$$

Taking into account Eq. (5) it is possible to eliminate the constraint matrix Λ , leading to the Bogoliubov equation

$$[\mathcal{H}(R), R] = 0\tag{9}$$

The Bogoliubov matrix \mathcal{H} in Eq. (9) is constructed with the help of the block matrices defined by Eq. (8). The explicit form of these matrix elements for the D1S effective interaction is given by references [28, 35]. The solution of Eq. (9) is then found by successive diagonalizations of the Bogoliubov Hamiltonian. This iterative solution method is described in greater detail in section II D and appendix A.

B. Basis truncation and aspects of one-center basis calculations

In practical applications, the formalism of section II A must be expressed in some basis. Typically, the deformed Harmonic-oscillator (HO) basis (see, e.g., chapter 2 in [27]) has been used in many HFB calculations, including those dealing with fission [4, 36]. The basis states in cylindrical coordinates (ρ, z, φ) are

$$\begin{aligned}\langle \vec{r} | n_r, \Lambda, n_z, \sigma \rangle &= \Phi_{n_r, |\Lambda|}(\rho; b_\perp) \frac{e^{i\Lambda\varphi}}{\sqrt{2\pi}} \\ &\times \Phi_{n_z}(z; b_z) \chi_\sigma\end{aligned}\tag{10}$$

where the explicit forms used in this work for the radial ($\Phi_{n_r, |\Lambda|}$) and Cartesian (Φ_{n_z}) components and their relevant properties can be found, e.g., in [35], and χ_σ is a spinor function for $\sigma = \pm 1/2$. These basis states assume axial symmetry of the nucleus explicitly. Other symmetries can also be imposed on the HFB calculation to reduce the overall size of the

problem. Two symmetries in particular are relevant to the fission calculations in this paper: the symmetry with respect to the parity operator $\hat{\Pi}$

$$\hat{\Pi} |n_r, \Lambda, n_z, \sigma\rangle = (-1)^{|\Lambda|+n_z} |n_r, \Lambda, n_z, \sigma\rangle$$

and the symmetry with respect to the z-signature operator $\hat{S}_z = i\hat{R}_z(\pi)$, where $\hat{R}_z(\pi)$ effects a rotation by π in both spatial and spin space,

$$\hat{S}_z |n_r, \Lambda, n_z, \sigma\rangle = \sigma(-1)^{|\Lambda|} |n_r, \Lambda, n_z, \sigma\rangle$$

Throughout this work, only the z-signature symmetry has been imposed, leaving the fissioning nucleus free to violate the symmetry with respect to parity and assume asymmetric shapes. These symmetries are taken into account explicitly by rewriting the general Bogoliubov transformation of Eq. (3) in terms of the relevant quantum numbers as

$$\begin{aligned} \eta_\mu^\dagger(q, s_z, \Omega) &\equiv \sum_n [U_{n\mu}^{q, s_z, \Omega} a_n^\dagger(q, s_z, \Omega) \\ &\quad + V_{n\mu}^{q, s_z, \Omega} a_n(q, s_z, \bar{\Omega})] \\ \eta_\mu(q, s_z, \bar{\Omega}) &\equiv \sum_n \left[\left(U_{n\mu}^{q, s_z, \bar{\Omega}} \right)^* a_n(q, s_z, \bar{\Omega}) \right. \\ &\quad \left. + \left(V_{n\mu}^{q, s_z, \bar{\Omega}} \right)^* a_n^\dagger(q, s_z, \Omega) \right] \end{aligned}$$

where q distinguishes protons and neutrons, $s_z = \pm 1$ is the z-signature quantum number, and $\bar{\Omega}$ is the total angular-momentum projection for the time-reversed state.

Even with the z-signature symmetry imposed, the treatment of fission can require large basis sizes and the calculation of a large number of two-body matrix elements. In order to further limit the size of problem, various basis truncation schemes have been devised. Some [37] keep only those basis states with corresponding HO energies below a given cutoff, while other schemes [4, 38] directly allow for more quanta along the z direction—the direction of elongation of the fissioning nucleus—compared to the radial direction. In the truncation scheme of [37], the HO quantum numbers must satisfy

$$\hbar\omega_\perp(n_\perp + 1) + \hbar\omega_z \left(n_z + \frac{1}{2} \right) \leq \hbar\omega_0(N + 2) \quad (11)$$

with $n_\perp \equiv 2n_r + |\Lambda|$ and for a given maximum shell number N , where the oscillator frequencies are related to the length parameters b_\perp and b_z in Eq. (10) by

$$\omega_\perp = \frac{\hbar}{mb_\perp^2}, \quad \omega_z = \frac{\hbar}{mb_z^2}, \quad \omega_0^3 = \omega_\perp^2 \omega_z \quad (12)$$

and m is the nucleon mass. With increasing axial elongation and for fixed N , Eq. (11) adds more shells in the z direction while simultaneously decreasing the number of shells in the radial direction, thus keeping the basis size from growing too quickly with deformation. In the truncation scheme of [4, 38], the condition

$$\frac{n_z}{q} + 2n_r + |\Lambda| \leq N \quad (13)$$

is imposed for a given maximum shell number N and parameter q . In this work we have used both truncation schemes. The truncation given by Eq. (11) has been used for most calculations in this paper, while the truncation of Eq. (13) has been used mainly in section III A.

The oscillator lengths b_\perp and b_z in Eq. (10), or equivalently the frequencies ω_\perp and ω_z , are variational parameters in the HFB calculation that must be chosen to minimize the HFB energy. Through a series of calculations in ^{240}Pu using the truncation scheme of Eq. (13) with $N = 13$ and $q = 1.5$, and exploring a wide range of values of the constraints on the quadrupole (Q_{20}) and octupole (Q_{30}) moments, an approximate dependence was obtained for the frequencies that minimize the HFB energy, given by

$$\hbar\omega_0 = 8.4345 - 0.0021668 Q_{20} \quad (14)$$

$$\frac{\omega_\perp}{\omega_z} = 1.7041 + 0.0028743 Q_{20} \quad (15)$$

with Q_{20} in barns and $\hbar\omega_0$ in MeV. No significant dependence on Q_{30} was observed in the range of interest.

Perhaps the most important aspect of the basis states in Eq. (10) is that they are centered about the origin by construction. In particular, the Gaussian factor in Eq. (10) ensures that the nuclear wave function falls off rapidly with increasing z . Despite this feature of the basis states, we will show that it is still possible to describe the exotic shapes occurring in fission. In order to describe both the neck (near $z = 0$) and nascent fragments (typically 5-10 fm from the origin) with the basis states of Eq. (10), we are forced to include many quanta in the z direction, and to use relatively large values of b_z .

To justify the use of the one-center basis for the range of fissioning configurations and quantities examined in this paper, we have performed separate HFB calculations for ^{134}Te and ^{106}Mo centered at the origin, and translated the resulting wave functions to the typical positions these nuclei occupy as ^{240}Pu nascent fission fragments. The formalism required for

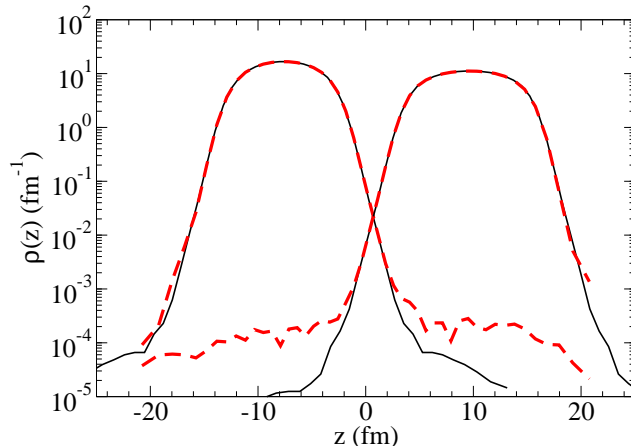


Figure 1: (Color online) Plots of the nuclear densities for fragments of ^{134}Te and ^{106}Mo along the axis of elongation of the nucleus, calculated in the one-center basis and plotted (as solid black lines) centered at $z = -7.63$ and 9.65 fm, respectively. The dashed red lines represent the same densities, but translated from the origin to their respective centroid positions within a finite harmonic-oscillator-basis truncated according to Eq. (11) and with $N=13$ shells, using the formalism in appendix B.

translating a wave function expressed within a finite HO basis is given in appendix B. The basis was truncated according to Eq. (11) with $N = 13$, resulting in a maximum number $n_z = 26$ along the z axis. The result is shown in Fig. 1, and compared to a translation in an infinite-sized basis (obtained in practice by redrawing the curves at the displaced centroid positions while preserving their shape). The comparison clearly shows the appearance of spurious tails for each fragment translated within a finite-size basis. If the fragments are separated further, e.g. by an additional 2.5 fm for each fragment in Fig. 2, the tails grow larger. However, the tails caused by the translation in a finite basis remain relatively small ($\sim 10^{-4} \text{ fm}^{-1}$ in Fig. 1, and $\sim 5 \times 10^{-4} \text{ fm}^{-1}$ in Fig. 2), and the separations between the fragments in both figures are larger than those encountered in the remainder of this work. In section III A we will show that these tails do not significantly affect the nuclear properties calculated in this paper. In a forthcoming publication [39] we will explore a more microscopic definition of scission and of the fission fragments, and we will calculate quantities such as the interaction energy between the fragments that may be more sensitively affected by the presence of these tails [43].

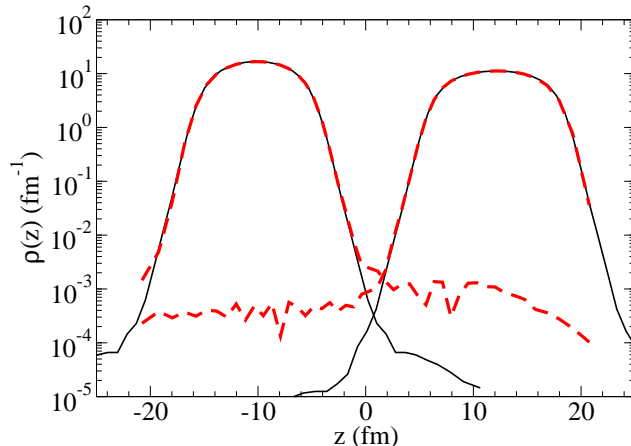


Figure 2: (Color online) Same as Fig. 1, but for the ^{134}Te and ^{106}Mo fragments translated an additional 2.5 fm each, to centroids at $z = -10.13$ and 12.15 fm, respectively.

C. Multiple constraints in HFB calculations

In this section, we focus on formal and practical considerations in the choice and control of multiple constraints in HFB calculations. We will describe a mechanism for the adjustment of the constraints which generalizes the discussion in [28]. The formalism described here and used in our calculations is that of variation with linear constraints. Other approaches for the adjustment of constraints, such as the quadratic-constraint method can also be found in the literature [40]. We have adopted the linear-variation approach in our work because we have found it to be stable and robust, and these are important qualities needed to map out the scission configurations, which requires precise control of the nuclear shape. For a process like fission, these constraints are central not only to being able to drive the nucleus to scission, but also to uncover the full richness of the microscopic method in its ability to describe the complexities of fission. In section II A we already discussed the introduction of constraints on the average number of neutrons and protons for the HFB Hamiltonian. Further constraints can be introduced through the external-field one-body operators $\lambda_i \hat{F}_i$,

$$H - \sum_i \lambda_i \hat{F}_i \quad (16)$$

where the parameters λ_i are used to adjust the field intensities. Based on Eq. (9), the Bogoliubov equation associated with Eq. (16) can now be written

$$\left[\mathcal{H}(R) - \sum_i \lambda_i \mathbb{F}_i, R \right] = 0$$

where

$$\mathbb{F}_i \equiv \begin{pmatrix} \hat{F}_i & 0 \\ 0 & -\hat{F}_i^* \end{pmatrix} \quad (17)$$

in the particle-hole representation, and $\mathcal{H}(R)$ is given by Eq. (8). In what follows, we will use the notation

$$\mathcal{H}(R, \{\lambda_i\}) \equiv \mathcal{H}(R) - \sum_i \lambda_i \mathbb{F}_i$$

where $\{\lambda_i\}$ represents the set of Lagrange multipliers other than those associated with the proton and neutron numbers. The λ_i Lagrange multipliers can be adjusted to yield an HFB solution with desired expectation values f_i of the fields

$$\begin{aligned} \langle \hat{F}_i \rangle &= \frac{1}{2} \text{Tr} \hat{F}_i + \frac{1}{2} \text{Tr} \mathbb{F}_i R \\ &= f_i \end{aligned}$$

The formalism used to find the appropriate λ_i parameters is derived in appendix A. In describing fission within the microscopic approach, we are free to impose any number of constraints, each defined by a corresponding external-field operator. We are limited in this task by the computational requirements, which grow quickly with the number of constraints, and by their relevance to the fission process.

In the simplest physical picture of fission, we expect that the nucleus will stretch along its symmetry axis until scission, and therefore introduce the mass quadrupole operator \hat{Q}_{20} as a constraint. Next, the octupole operator \hat{Q}_{30} is introduced to account for the range of mass divisions observed in fragments, from symmetric to asymmetric. With the introduction of the octupole constraint, we are forced to impose a constraint on the dipole moment, \hat{Q}_{10} , as well in order to maintain the center of mass of the nucleus fixed. The hexadecapole operator \hat{Q}_{40} controls the formation of the neck between nascent fragments, and accounts for the range of fission modes from cold to hot [2]. In addition, we recall that the HFB procedure

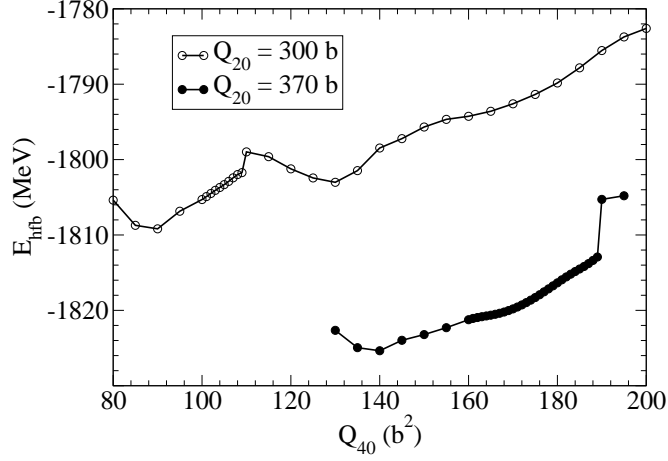


Figure 3: Calculated HFB energy for ^{240}Pu as a function of hexadecapole moment, and for quadrupole moments of 300 b (cold fission) and 370 b (hot fission). For the $\langle Q_{20} \rangle = 300$ b case, the fission valley is seen near $\langle \hat{Q}_{40} \rangle = 130$ b 2 , and the fusion valley is near $\langle \hat{Q}_{40} \rangle = 90$ b 2 . For the $\langle Q_{20} \rangle = 370$ b case, only the fusion valley is observed, near $\langle \hat{Q}_{40} \rangle = 140$ b 2 .

requires constraints on the expected values of the proton-number (\hat{N}_p) and neutron-number (\hat{N}_n) operators.

In Fig. 3, we show a calculation of the HFB energy for ^{240}Pu as a function of Q_{40} ($Q_{40} \equiv \langle \hat{Q}_{40} \rangle$) at two quadrupole deformations, 300 b and 370 b, which correspond to the so-called cold and hot fission limits, respectively [2]. These calculations were performed with 5 constraints (for the values of $\langle \hat{N}_p \rangle = 94$, $\langle \hat{N}_n \rangle = 146$, $\langle \hat{Q}_{10} \rangle = 0$, $\langle \hat{Q}_{20} \rangle = 300$ b or 370 b, and $80 \text{ b}^2 \leq \langle \hat{Q}_{40} \rangle \leq 200 \text{ b}^2$). In the cold-fission case, a barrier of height ~ 4.0 MeV relative to the fission-valley minimum separates the two valleys. Near the hot-fission limit, the fission valley has disappeared and the nucleus spontaneously falls into the fusion valley near $\langle \hat{Q}_{40} \rangle = 140$ b 2 . Between the hot and cold extremes, the nucleus can undergo fission through a range of intermediate modes.

The energy curves plotted in Fig. 3 effectively represent slices at fixed values of $\langle \hat{Q}_{40} \rangle$ in Fig. 3 of [2]. The most striking feature in Fig. 3 is the sudden variation in energy over a very small step size in $\langle \hat{Q}_{40} \rangle$ of 1 b 2 . In the cold-fission case, a drop of 2.7 MeV is observed in going from $\langle \hat{Q}_{40} \rangle = 110$ b 2 to 109 b 2 , and in the hot-fission case a more pronounced drop of 7.6 MeV occurs in going from $\langle \hat{Q}_{40} \rangle = 190$ b 2 to 189 b 2 . These abrupt changes in energy, which are in contrast to the smooth behavior displayed in [2], correspond to a sudden

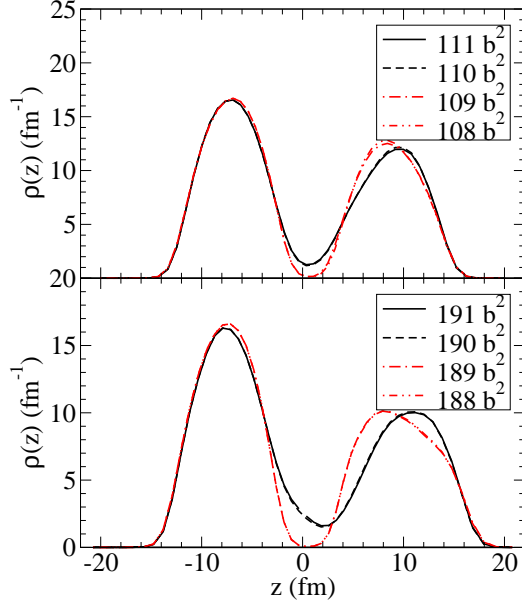


Figure 4: (Color online) Calculated nuclear densities in steps of $\Delta \langle \hat{Q}_{40} \rangle = 1 \text{ b}^2$ around the scission configuration for cold (top panel) and hot (bottom panel) fission. The legends give the values of $\langle \hat{Q}_{40} \rangle$ for the different curves.

reduction in the neck size (Fig. 4), which we take as an indicator of a transitional phase where the nucleus is undergoing scission. Note that the identification of such transitional phases requires extremely small variations of the constraints, which could explain why they were not seen in [2]. The precise control of the constraints needed to study the region around scission is one of the important points that emerges from the work presented in this paper, and the motivation for going into some detail in the description of the constraint-adjustment algorithm in the next section and in appendix A.

The rapid change of the neck size mentioned above suggests the introduction of a constraint proportional to the average number of particles $\langle \hat{Q}_N \rangle$ in the neck separating the nascent fragments, where [4]

$$\hat{Q}_N \equiv \exp \left[-\frac{(z - z_N)^2}{a_N^2} \right] \quad (18)$$

with $a_N = 1 \text{ fm}$, and z_N is the position of the neck (defined as the point between the fragments where the matter density is lowest). As shown in Fig. 5, the energy calculated as a function of $\langle \hat{Q}_N \rangle$ becomes smoother and continuous. A more detailed discussion of this result is given in the latter part of section II D.

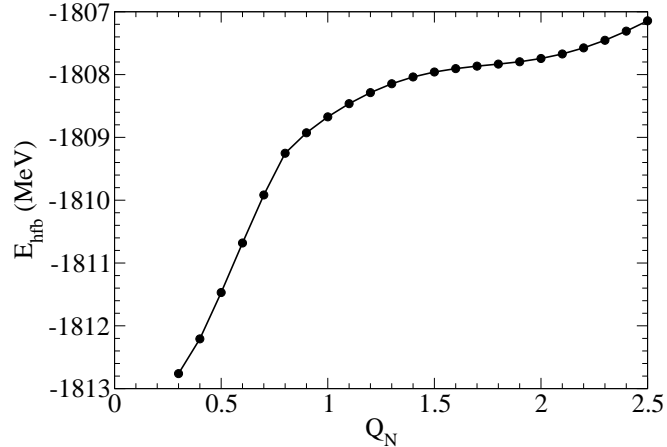


Figure 5: Variation of the HFB energy as a function of the number of particles in the neck, defined by Eq. (18), at the scission configuration ($\langle \hat{Q}_{40} \rangle = 189 \text{ b}^2$) for the hot-fission calculation ($\langle \hat{Q}_{20} \rangle = 370 \text{ b}$) in Fig. 3.

D. The HFB convergence algorithm

The control of HFB calculations with multiple constraints is a delicate procedure, made difficult by the number of constraints and their inherent correlations. Because the topic continues to be of current interest in problems that rely on constrained-HFB methods even beyond fission [32, 41], the convergence algorithm used in the present HFB calculations is discussed in detail here. The algorithm must balance, at each iteration, the diagonalization of the HFB Hamiltonian to ensure self-consistency, and adjustment of the Lagrange multipliers in Eq. (16). The main steps of the algorithm are as follows

1. Read initial generalized density R and Lagrange multipliers λ_i
2. Construct constrained HFB Hamiltonian $\mathcal{H}(R, \{\lambda_i\})$
3. Diagonalize $\mathcal{H}(R, \{\lambda_i\})$
4. Construct new R
5. Mix R between consecutive iterations using a mixing parameter α (see Eq. (20))
6. Adjust value of α based on convergence criterion

7. Calculate $\delta\lambda_i$ needed to yield desired constraint values, adjust λ_i
8. Calculate δR corresponding to the $\delta\lambda_i$, adjust R
9. If HFB solution is not converged, return to step 2

The first 4 steps in this algorithm are fairly self-explanatory and make use of the formalism derived in section II A. We will examine the remaining steps in greater detail since they are not typically discussed in depth in the literature.

At the end of each iteration i , the convergence of the HFB solution is assessed by calculating the largest variation from the previous iteration in the elements of the generalized density matrix,

$$\varepsilon_i \equiv \sup |R_{mn}^{pq}(i) - R_{mn}^{pq}(i-1)| \quad (19)$$

The quantity ε_i is also used to determine the coefficient α in step 5 which mixes the generalized densities between successive iterations using an adjustable coefficient α ,

$$R_{mn}^{pq}(i) \rightarrow (1 - \alpha) R_{mn}^{pq}(i) + \alpha R_{mn}^{pq}(i-1) \quad (20)$$

with $0 \leq \alpha \leq 1$. This mixing is essential to slow down the convergence algorithm which would otherwise often behave erratically in the first few iterations and could fail to converge at all. The mixing coefficient α is adjusted in step 6 in such a way that it tends to zero as ε_i decreases. In practice, two thresholds are supplied, ε_{min} and ε_{max} , along with a maximum value α_{max} for the mixing coefficient such that

$$\alpha = \begin{cases} \alpha_{max} & \varepsilon_i \geq \varepsilon_{max} \\ \alpha_{max} \frac{\varepsilon_i - \varepsilon_{min}}{\varepsilon_{max} - \varepsilon_{min}} & \varepsilon_{min} < \varepsilon_i < \varepsilon_{max} \\ 0 & \varepsilon_i \leq \varepsilon_{min} \end{cases}$$

Furthermore, if the HFB solution diverges from one iteration to the next (i.e., if $\varepsilon_i > \varepsilon_{i-1}$) then α is set to α_{max} and remains at that value until the HFB solution converges again. For the work in this paper we have used $\varepsilon_{min} = 10^{-3}$ or 10^{-4} , $\varepsilon_{max} = 10^{-1}$, and $\alpha_{max} = 0.5$ (or in a few cases 0.8 for a slower initial convergence). We note in passing that the mixing of generalized density matrices is a global operation, i.e. the same coefficient α is used for all the matrix elements. The Broyden method, or its more elaborate modified version

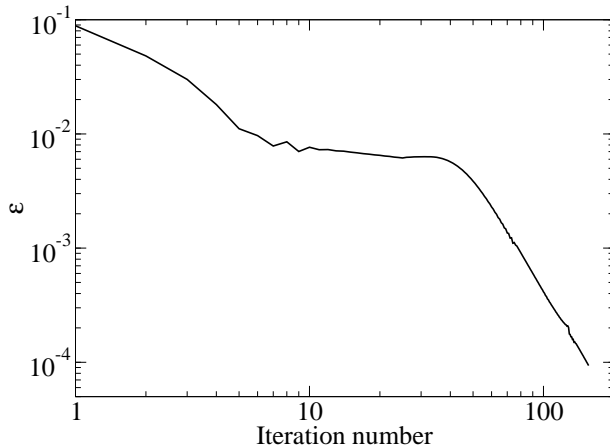


Figure 6: Plot of the convergence metric, given by Eq. (19), as a function of HFB iteration number for the $\langle \hat{Q}_{40} \rangle = 110 \text{ b}^2$ cold-fission point in Fig. 3.

[41], could provide a better alternative for optimizing the choice of the mixing coefficient by associating an independent value of α to each matrix element.

The formalism needed to adjust the Lagrange parameters in step 7, and the generalized density in step 8 is presented in appendix A, and we stress the importance of adjusting both for a stable convergence of the HFB method. The algorithm is considered to have converged in step 9 if $\varepsilon_i \leq \varepsilon_{min}$ for several iterations (typically 2 in the present work).

In order to illustrate various aspects of the convergence algorithm, we have examined the cold-fission point at $\langle \hat{Q}_{40} \rangle = 110 \text{ b}^2$ in Fig. 3 in detail. Because this point corresponds to a local maximum in the HFB energy, its calculation is particularly demanding on the convergence algorithm. In Fig. 6 we show the convergence criterion, ε , calculated using Eq. (19) at each iteration. The HFB solution is found to better than $\varepsilon < 10^{-4}$ after 156 iterations in this case. We note a region in Fig. 6 roughly between iterations 10 and 40, where ε appears to be relatively constant and the convergence is correspondingly slow. In this region, all the constraints appear to be close to their desired values, except for the dipole moment. The $\langle \hat{Q}_{10} \rangle$ value is still relatively large ($\sim 0.06 - 0.2 \text{ fm}$) and may be responsible for the stagnant convergence.

In Fig. 7 we examine the adjustment of the five constraints at each iteration. The figure shows the relative deviation of each constraint from the desired value. For all but the dipole-moment constraint, this relative deviation of the calculated average value $\langle \hat{Q} \rangle$ of the

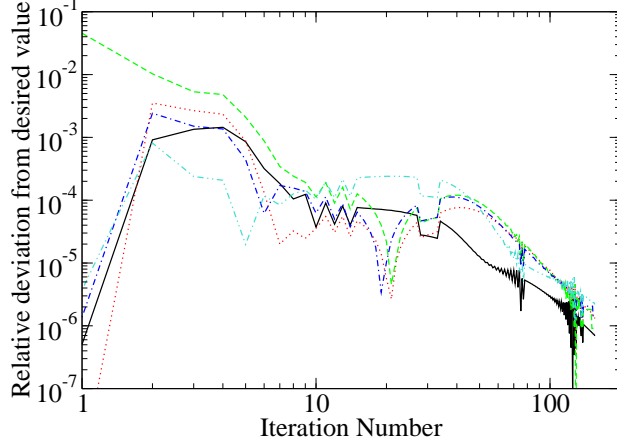


Figure 7: (Color online) Relative deviations of the calculated constraint values from their desired values as a function of HFB iteration number for the calculation with $\langle \hat{Q}_{40} \rangle = 110 \text{ b}^2$. The relative deviation for the dipole moment is given by Eq. (22), and by Eq. (21) for all other constraints. The constraints shown are: $\langle \hat{Q}_{10} \rangle$ (black solid line), $\langle \hat{Q}_{20} \rangle$ (red dotted line), $\langle \hat{Q}_{40} \rangle$ (green dashed line), $\langle \hat{N}_n \rangle$ (blue dot-dashed line), and $\langle \hat{N}_p \rangle$ (turquoise dot-dot-dashed line).

constraint from its desired value q is given by

$$\left| \frac{\langle \hat{Q} \rangle - q}{q} \right| \quad (21)$$

In the case of the dipole moment, the desired value is $q_{10} = 0$ and Eq. (21) cannot be used. Instead, we obtain from $\langle \hat{Q}_{10} \rangle$ the position of the centroid of the nucleus, given by $\langle \hat{Q}_{10} \rangle / A$ where $A = 240$ is the total number of nucleons, and compare it to the calculated root-mean-squared radius of the nucleus, R_{rms} , using the ratio

$$\left| \frac{\langle \hat{Q}_{10} \rangle}{AR_{rms}} \right| \quad (22)$$

The calculation is started from an HFB solution that differs only in the value of the hexadecapole constraint, $\langle \hat{Q}_{40} \rangle = 115 \text{ b}^2$, with all other constraints the same. Hence we see in Fig. 7 that at the first iteration, all relative deviations except the one for the hexadecapole-moment constraint are small. The calculation converges to the desired level of accuracy after 156 iterations.

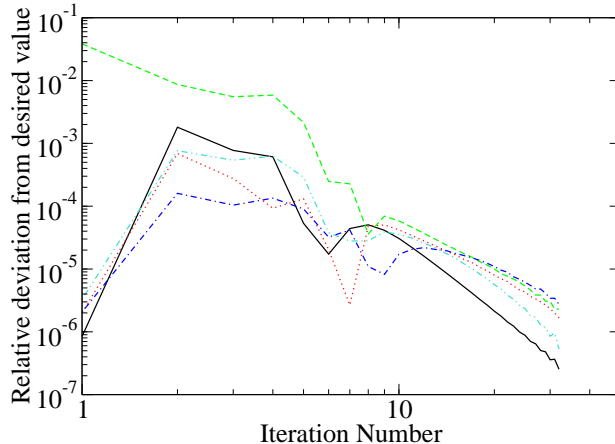


Figure 8: (Color online) Same as Fig. 7, but for the calculation with $\langle \hat{Q}_{40} \rangle = 130 \text{ b}^2$.

This difficult convergence should be contrasted with the calculation of the cold-fission point at $\langle \hat{Q}_{40} \rangle = 130 \text{ b}^2$, near the bottom of the fission valley in Fig. 3. The relative deviations of the constraints for this more stable calculation are shown in Fig. 8. After the tenth iteration, all constraints tend to the desired value rapidly and smoothly. This calculation is converged to the same level of accuracy as the one at $\langle \hat{Q}_{40} \rangle = 110 \text{ b}^2$ after only 33 iterations.

Finally, we discuss in greater detail the discontinuities observed in Fig. 3. Such discontinuities have been alluded to in the literature [42] as a potential difficulty for microscopic calculations. In this section, we show how these discontinuities are an indicator of a change in the meaning of certain collective coordinates near the critical scission configurations. We also show how these discontinuities can be eliminated through the choice of a more appropriate collective coordinate.

The impact of these discontinuities can be felt even before the scission configuration is reached. We illustrate this point by showing the results of HFB calculations, performed with identical multipole constraints up to the hexadecapole moment (i.e., with the same $\langle \hat{Q}_{10} \rangle$, $\langle \hat{Q}_{20} \rangle$, $\langle \hat{Q}_{30} \rangle$, $\langle \hat{Q}_{40} \rangle$ values), but different initial densities. We will approach the cold-fission scission configuration near $\langle \hat{Q}_{40} \rangle = 110 \text{ b}^2$ in Fig. 3 with an initial density corresponding to either a scissioned or non-scissioned nucleus. The first calculation, shown in Fig. 9, was performed at $\langle \hat{Q}_{40} \rangle = 130 \text{ b}^2$, near the bottom of the fission valley. Two curves

are shown, corresponding to a initial choice of the generalized density calculated at $\langle \hat{Q}_{40} \rangle = 135 \text{ b}^2$ (whole nucleus), and $\langle \hat{Q}_{40} \rangle = 90 \text{ b}^2$ (broken/scissioned nucleus). As expected, both choices of starting point lead to exactly the same HFB solution, as is evidenced by the overlapping density curves in Fig. 9. By contrast, Fig. 10 compares calculations at $\langle \hat{Q}_{40} \rangle = 115 \text{ b}^2$ (i.e., near scission), starting from solutions at $\langle \hat{Q}_{40} \rangle = 120 \text{ b}^2$ (whole) and $\langle \hat{Q}_{40} \rangle = 90 \text{ b}^2$ (broken). Both solutions have the same values of the first four moments, yet the calculation started from a whole solution leads to a whole result, while the broken starting configuration leads to a broken-nucleus solution. A similar effect is observed in Fig. 11, corresponding to a calculation very close to scission at $\langle \hat{Q}_{40} \rangle = 110 \text{ b}^2$ with starting densities from $\langle \hat{Q}_{40} \rangle = 115 \text{ b}^2$ (whole) and $\langle \hat{Q}_{40} \rangle = 90 \text{ b}^2$ (broken) solution. Note that these HFB calculations are performed with an unprecedented 7 simultaneous constraints.

The densities plotted in Figs. 9-11 reveal a complex relationship between the hexadecapole and Q_N degrees of freedom. These two coordinates are not related by a one-to-one mapping and cannot be used interchangeably to drive the system to scission. In Fig. 12 we show the HFB energy surface as a function of Q_{40} and Q_N for the calculation with all moments up to hexadecapole fixed. In particular, $\langle \hat{Q}_{20} \rangle = 300 \text{ b}$, and $\langle \hat{Q}_{30} \rangle = 34.951 \text{ b}^{3/2}$ —the value of the octupole moment for the two calculations in Fig. 11. The shape of the energy surface suggests that energy-minimizing HFB solutions can exist which have the same value of $\langle \hat{Q}_{40} \rangle$, but distinct values of $\langle \hat{Q}_N \rangle$. For most—but not all—values of $\langle \hat{Q}_{40} \rangle$ a small barrier in the surface (marked by a solid line along the surface in the figure) separates the minima with differing values of $\langle \hat{Q}_N \rangle$. This barrier is at best a few hundred keV's high and decreases rapidly with decreasing $\langle \hat{Q}_{40} \rangle$ as we approach the scission configuration. At $\langle \hat{Q}_{40} \rangle = 110 \text{ b}^2$ the barrier has dropped to only 1.8 keV and vanishes completely between $\langle \hat{Q}_{40} \rangle = 104 \text{ b}^2$ and 110 b^2 . This break in the barrier causes the discontinuity in Fig. 3, where the calculations are performed without a constraint on $\langle \hat{Q}_N \rangle$ to prevent the HFB calculation from falling into the scissioned configuration.

Near scission, the total multipole moments of the nucleus are determined by the intrinsic and relative moments of the fragments, and rearrangements between these terms can produce different matter distributions with the same overall moments, at least up to the hexadecapole. Thus imposing a constraint on $\langle \hat{Q}_{40} \rangle$ will not necessarily result in a constraint on the neck size near scission. The $\langle \hat{Q}_N \rangle$ constraint on the other hand was already shown

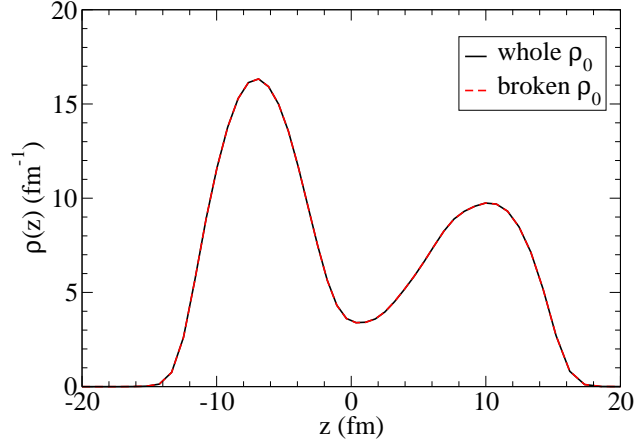


Figure 9: (Color online) Comparison of nuclear densities for the $\langle \hat{Q}_{40} \rangle = 130 \text{ b}^2$ cold-fission point in Fig. 3, starting either from a whole (solid black line) or scissioned/broken (dashed red line) initial configuration of the nuclear density in the HFB iterations. All moments up to the hexadecapole have been constrained to the same values for the two calculations.

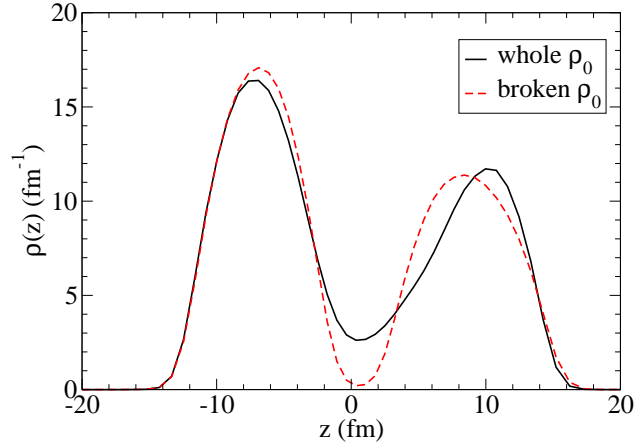


Figure 10: (Color online) Same as Fig. 9, but for a calculation at $\langle \hat{Q}_{40} \rangle = 115 \text{ b}^2$.

to produce a smooth energy dependence in Fig. 5 and is therefore the suitable coordinate in the study of fission for configurations near and beyond scission.

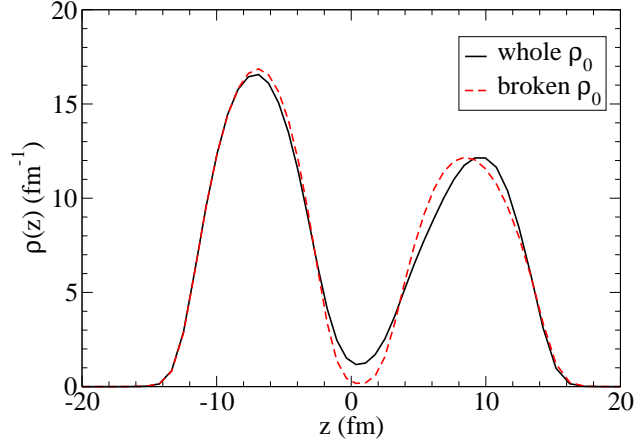


Figure 11: (Color online) Same as Fig. 9, but for a calculation at $\langle \hat{Q}_{40} \rangle = 110 \text{ b}^2$.

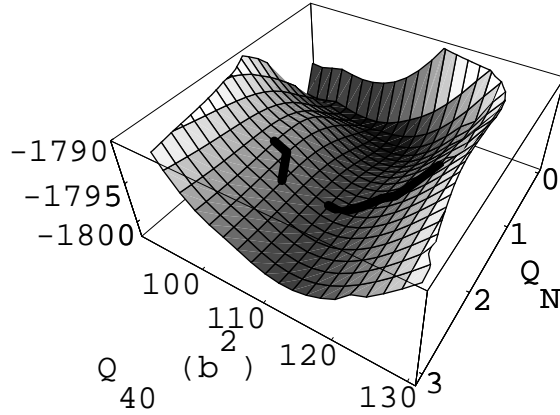


Figure 12: Energy surface calculated with constraints on $\langle \hat{N}_n \rangle = 146$, $\langle \hat{N}_p \rangle = 94$, $\langle \hat{Q}_{10} \rangle = 0$, $\langle \hat{Q}_{20} \rangle = 300 \text{ b}$, $\langle \hat{Q}_{30} \rangle = 34.951 \text{ b}^{3/2}$, $90 \text{ b}^{3/2} \leq \langle \hat{Q}_{40} \rangle \leq 130 \text{ b}^{3/2}$, and $0.05 \leq \langle \hat{Q}_N \rangle \leq 3.05$. The dark lines along the surface mark the position of a small local barrier on the surface.

E. Scission in the constrained-HFB approach

In this section, we briefly discuss various signatures of scission. Some of the characteristics of scission have already been mentioned in sections II C and II D. The standard indicators of scission are sudden changes in either energy (interaction energy between fragments or total HFB energy) or shape (neck size or hexadecapole moment) for the nucleus [14]. For the work in this paper, we use the same semiclassical definition of the nascent fission fragments

as in [14], where a position along the symmetry axis of the nucleus is identified as a divider between left and right fragments, and the fragment properties are obtained as integrals over the density with this cut as an endpoint for the integrals. In a forthcoming publication [39], we will adopt a more microscopic criterion to identify the fragment [43], based on the individual single-particle wave functions, and using the changes in the interaction energy between fragments as an indicator of scission. In this paper we will focus instead on the HFB energy and the number of particles in the neck before and after scission.

Consider, for example, the cold-fission calculation in Fig. 3. At $\langle \hat{Q}_{40} \rangle = 110 \text{ b}^2$ there is still a significant amount of matter in the neck connecting the nascent fragment with $\langle \hat{Q}_N \rangle = 2.41$. At $\langle \hat{Q}_{40} \rangle = 109 \text{ b}^2$ however, the neck breaks and $\langle \hat{Q}_N \rangle$ drops to 0.50 particles. This sudden variation in shape over a small increment in hexadecapole moment is shown in the top panel of Fig. 4. At $\langle \hat{Q}_{40} \rangle = 90 \text{ b}^2$, the bottom of the fusion valley, $\langle \hat{Q}_N \rangle$ has been reduced to 0.09 particles. From $\langle \hat{Q}_{40} \rangle = 110 \text{ b}^2$ to 109 b^2 , the total HFB energy drops by 2.7 MeV, and the difference in energy between $\langle \hat{Q}_{40} \rangle = 110 \text{ b}^2$ and 90 b^2 is 10.2 MeV.

A similar analysis can be performed for the hot-fission calculation in Fig. 3. In this case, the last point where a sizable neck still exists between the nascent fragment is at $\langle \hat{Q}_{40} \rangle = 190 \text{ b}^2$, with $\langle \hat{Q}_N \rangle = 2.92$ particles. By $\langle \hat{Q}_{40} \rangle = 189 \text{ b}^2$ the neck has essentially disappeared, and $\langle \hat{Q}_N \rangle$ has dropped to 0.23 particles. At the bottom of the fusion valley, where $\langle \hat{Q}_{40} \rangle = 140 \text{ b}^2$, there are only $\langle \hat{Q}_N \rangle = 0.02$ particles in the neck. The change in shape is plotted in the bottom panel of Fig. 4. The drops in energy are more significant than in the cold-fission case. From $\langle \hat{Q}_{40} \rangle = 190 \text{ b}^2$ to 189 b^2 , the total HFB energy drops by 7.6 MeV, and from $\langle \hat{Q}_{40} \rangle = 190 \text{ b}^2$ to 140 b^2 , it drops by 20.1 MeV.

III. RESULTS

A. Benchmark: ^{226}Th scission

We have performed HFB calculations of hot-fission properties for ^{226}Th , in order to compare with the results in [14] that were obtained with two-center HFB calculations. We have used both the basis truncation of Eq. (13) with $N = 13$ and $q = 1.5$, and the one given by Eq. (11) with $N = 13$. The oscillator-frequency parametrization of Eqs. (14) and

(15) was used, even though it was obtained for calculations in ^{240}Pu . We will show that our results are in good agreement with those of Dubray *et al.* [14] for ^{226}Th with either basis truncation scheme.

In Fig. 13, we plot the hot-scission line for ^{226}Th , and compare it to the one obtained in [14]. The scission line was determined by performing series of calculations at fixed $\langle \hat{Q}_{30} \rangle$ and increasing values of $\langle \hat{Q}_{20} \rangle$ by 5 b, each calculation using the previous one as a starting point, until an HFB solution was found where the neck size decreased drastically. Lines separated by $\Delta \langle \hat{Q}_{20} \rangle = 5$ b connecting the HFB solutions just before and just after the breaking of the neck are displayed in Fig. 13, bracketing the actual scission line. These lines are in good agreement with the ^{226}Th scission line in [14]. In Fig. 14 we examine the region with $\langle \hat{Q}_{30} \rangle = 25 - 35 \text{ b}^{3/2}$ in greater detail. A series of HFB calculations were performed at constant $\langle \hat{Q}_{20} \rangle$ values of 280, 310, 360, and 400 b starting from $\langle \hat{Q}_{30} \rangle = 25 \text{ b}^{3/2}$ in each case and proceeding in steps of $\Delta \langle \hat{Q}_{30} \rangle = 1 \text{ b}^{3/2}$. For these calculations, the basis truncation of Eq. (11) was used with $N = 13$ in order to provide a larger number of oscillator shells (up to 26 in practice) in the z direction, while keeping the overall number of basis states relatively low. With these large-basis calculations, we find that the results of Dubray *et al.* [14] are very well reproduced.

In Fig. 15, we compare the mass quadrupole moment calculated for the fragments for the HFB solutions just before scission (solid disks connected by solid lines in Fig. 13) to the corresponding result in [14]. As in [14], the Q_{20} values were calculated by integration over the left- and right-fragment densities, truncated at the neck position. The results of [14] are well reproduced by our calculations. Similarly, in Fig. 16, we show the octupole moment of the fragments compared to the Dubray *et al.* results. In this case as well, the agreement between the two sets of calculations is good.

The agreement between one-center and two-center calculations in Figs. (13)-(16) is reassuring, both as a benchmark for the HFB code used in this work, and as an assessment of the applicability of the one-center basis near scission. With these results in mind, we turn next to the fission properties of ^{240}Pu .

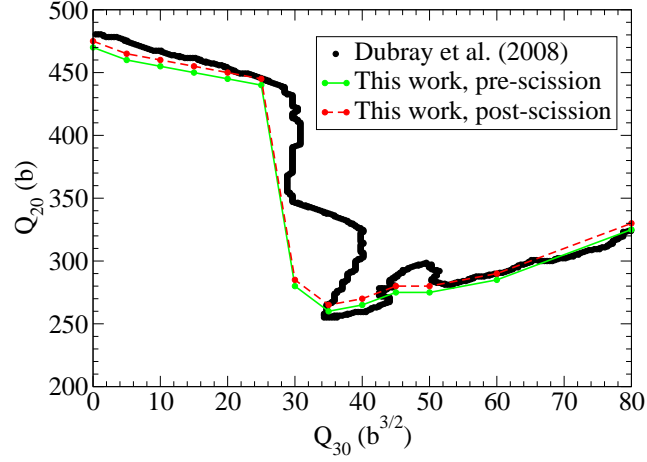


Figure 13: (Color online) Scission line for ^{226}Th obtained in this work, and compared to the result of Dubray *et al.* [14]. The solid disks connected by a solid green line represent HFB solutions just before scission in this work, and the solid disks connected by a dashed red line represent solutions immediately after scission in this work. The thick solid black curve is the scission line taken from [14].

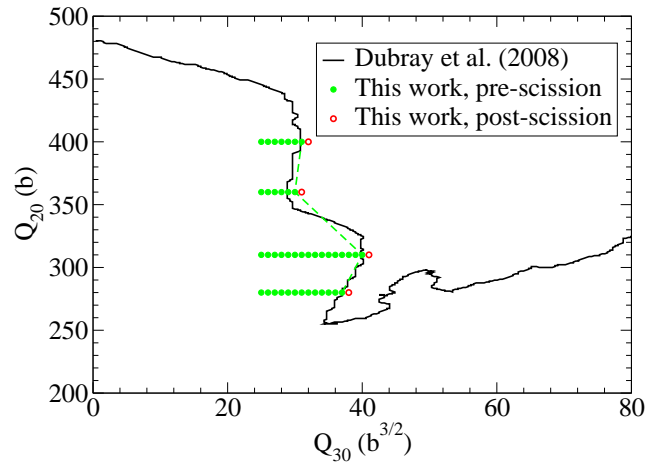


Figure 14: (Color online) Large-basis HFB calculations in ^{226}Th along lines with fixed $\langle \hat{Q}_{20} \rangle$ performed to reproduce the details of the scission line found in Dubray *et al.* [14]. A dashed line connects the last point before scission, and should be compared to the Dubray *et al.* result (solid line).

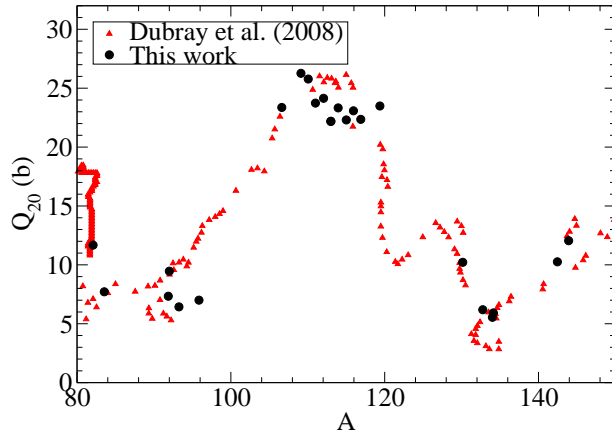


Figure 15: (Color online) Comparison of fission-fragment quadrupole moments as a function of fragment mass number between this work (solid black disks) and the results in [14] (solid red triangles).

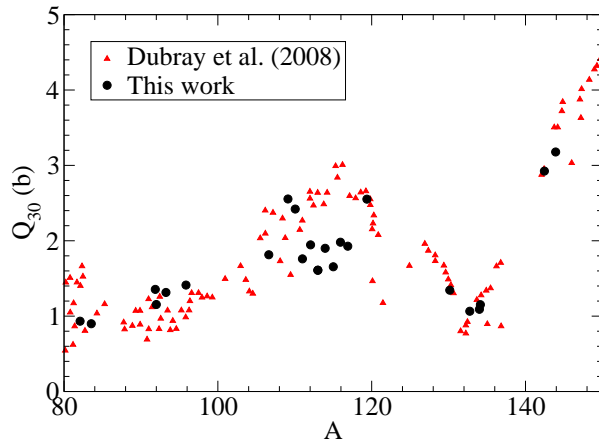


Figure 16: (Color online) Same as Fig. 15, but for the fission-fragment octupole moments.

B. ^{240}Pu scission

For the ^{240}Pu calculations, we have used the truncation scheme of Eq. (11) with $N = 13$. The parameterization in Eqs. (14) and (15) was adopted for the HO frequencies.

Fig. 17 illustrates the search for the hot-scission line in ^{240}Pu . Points along lines with fixed $\langle \hat{Q}_{30} \rangle$ or $\langle \hat{Q}_{20} \rangle$ increasing in steps of $1 \text{ b}^{3/2}$ and 5 b near the scission line, respectively, denote individual HFB calculations, each using the previous one as a starting point. As in

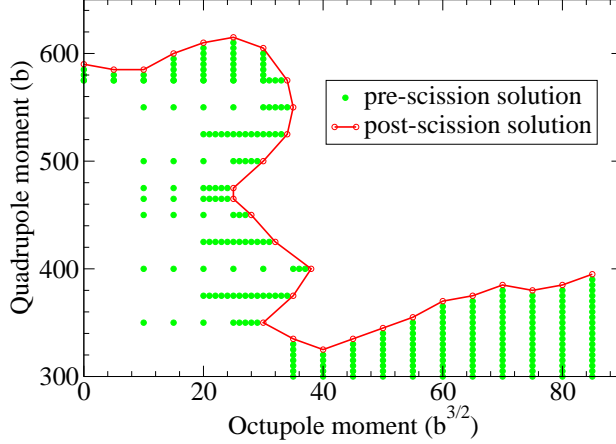


Figure 17: (Color online) Scission line for ^{240}Pu obtained in this work. All calculations were done using the basis truncation of Eq. (11). The solid green disks represent HFB calculations producing a whole (non-scissioned) nuclear density. The empty red circles connected by a solid line represent scissioned configurations.

the case of ^{226}Th in Fig. 13, the nucleus tends to stretch to much larger deformations in the symmetric limit. This leads to fragments that are formed much further apart in symmetric fission, and a corresponding drop in their mutual Coulomb repulsion—and therefore their total kinetic energy—as observed experimentally [44]. As in the case of ^{226}Th , we also observe regions around $Q_{20} = 550 \text{ b} / Q_{30} = 35 \text{ b}^{3/2}$ and $Q_{20} = 400 \text{ b} / Q_{30} = 38 \text{ b}^{3/2}$ where the scission line “bulges out”. In these regions, for a given Q_{30} value, the nucleus may scission at more than one value of Q_{20} .

Fig. 18 compares the total HFB energy of the fissioning nucleus just before and just after scission. In general, scission is accompanied by a marked drop in HFB energy. That drop, however, is much more pronounced for fission near the symmetric limit, where it can be as large as $\sim 50 \text{ MeV}$ over the $\Delta \langle \hat{Q}_{20} \rangle = 5 \text{ b}$ change in quadrupole moment. Note that the fragment masses in Fig. 18 are not the same before and after scission. This difference is an indication of the drastic variations in the nuclear density, and the redistribution of particles in the neck between the two fragments at scission.

The number of particles in the neck just before and after scission is shown in Fig. 19 as a function of the heavy-fragment mass. The variation in $\langle \hat{Q}_N \rangle$ is quite large (typically by an order of magnitude, but near the symmetric limit, by more than a factor of 1000).

As in [14], we extract the fragment properties for each mass division from the HFB calcu-

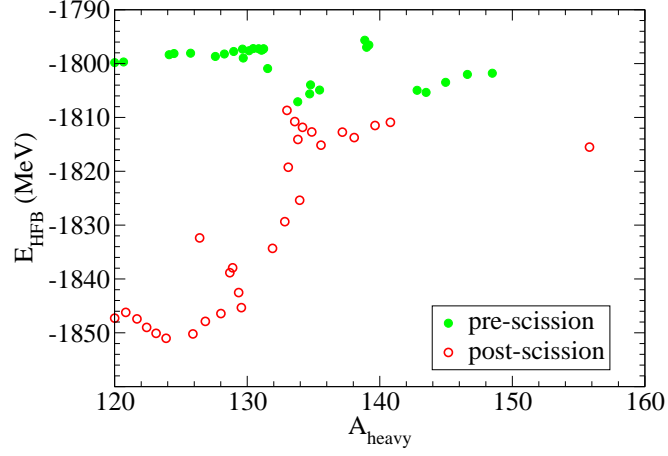


Figure 18: (Color online) HFB energy of the fissioning nucleus, plotted as a function of the heavy-fragment mass number, obtained from the HFB calculations just before (solid green disks) and just after (empty red circles) scission in Fig. 17.

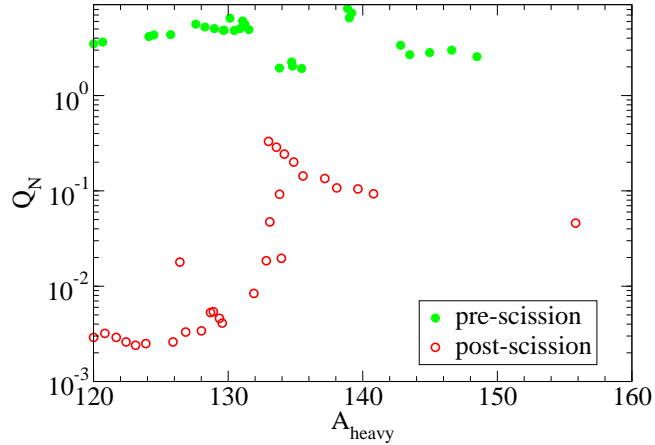


Figure 19: (Color online) Number of particles in the neck of the fissioning nucleus, plotted as a function of the heavy-fragment mass number, obtained from the HFB calculations just before (solid green disks) and just after (empty red circles) scission in Fig. 17.

lation just before scission. However, we go further than the calculation in [14] by attempting to approach the scission configuration even more closely. We introduce an additional constraint on Q_N to each point in the $Q_{20} - Q_{30}$ map of Fig. 17 just before the scission line, and search for the Q_N value marking a point just before a drop in E_{HFB} occurs. Fig. 20

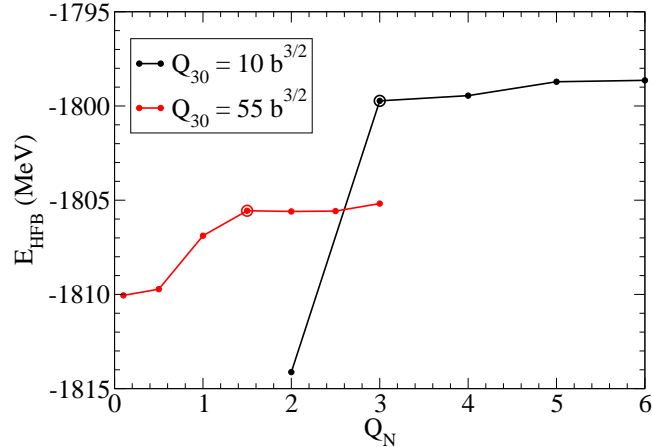


Figure 20: (Color online) Identification of the last configuration before scission for HFB calculations at fixed $Q_{30} = 10 \text{ b}^{3/2}$ and $55 \text{ b}^{3/2}$, as a function of the Q_N constraint. The circled points on each curve were chosen as the last pre-scission configuration, before the drop in HFB energy as a function of decreasing Q_N .

shows some typical choices for this point. In Fig. 21, the charge and mass of each fragment is plotted, covering a range from $A = 93$ to 147. We note that there is a nearly linear relationship between the mass and charge of the fragments, which can be fitted as

$$Z = 3.5349 + 0.36221 A$$

This result is consistent with the prediction of the Unchanged-Charge Division (UCD) model [45], also shown in Fig. 21 for comparison, which for ^{240}Pu yields

$$Z = \frac{94}{240} A \approx 0.3917 A$$

The moments of the fragments are shown in Figs. 22-24. The overall shape of the quadrupole moment in Fig. 22 is similar to the one shown for ^{226}Th in Fig. 15, with a maximum at the symmetric limit, and a drop-off on either side. There is also a significant dip in the $\langle \hat{Q}_{20} \rangle$ value near the nearly-spherical ^{134}Te fragment. The fragment octupole moment, plotted in Fig. 23, also shows similarities in shape as well as magnitude to the ^{226}Th case in Fig. 16 [46]. Finally, we also show the hexadecapole moment of the fragments in Fig. 24. There as well, the value of $\langle \hat{Q}_{40} \rangle$ reaches a maximum near the symmetric limit, and drops off on either side. In all cases, a line has been drawn to guide the eye using a

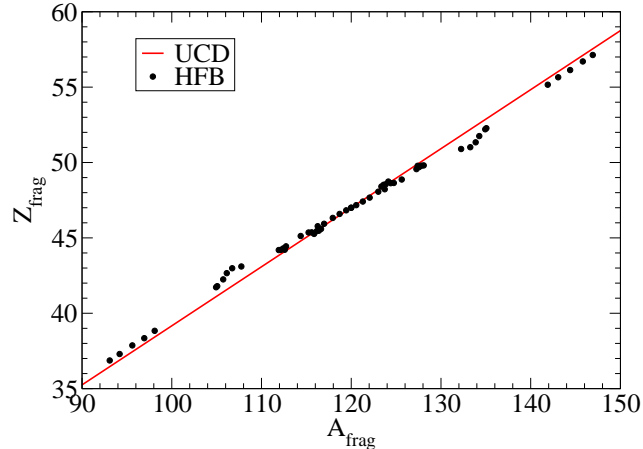


Figure 21: (Color online) Fission-fragment charge number plotted as a function of mass number, obtained from the HFB calculations immediately prior to scission in Fig. 17. The UCD prediction (solid red line) is plotted for comparison.

polynomial fit to the points. The HFB calculations in Figs. 22-24 exhibit a great deal of fluctuation about the smooth polynomial fit. These fluctuations are due for the most part to the difficulty in identifying a scission configuration based on the criterion of sudden changes in global nuclear properties, such as the total energy. In a forthcoming paper [39], we will embark on a more detailed study of the scission configurations at the microscopic level, and extract the excitation, kinetic, and interaction energies of the fragments. The merits and difficulties of a scission criterion based on the interaction energy between the fragments will be discussed in detail.

IV. CONCLUSION

We have developed the HFB code FRANCHBRIE for microscopic fission studies using the finite-range D1S effective interaction. The code allows for the multiple constraints needed to explore the nuclear densities relevant to fission, and is based on matrix elements calculated in a one-center deformed harmonic-oscillator basis. We have provided a detailed derivation of the formalism required for the adjustment of those multiple constraints.

We have applied the code to the calculation of scission configurations in the hot fission of ^{240}Pu . These calculations are relevant to studies of thermal neutron-induced fission on a

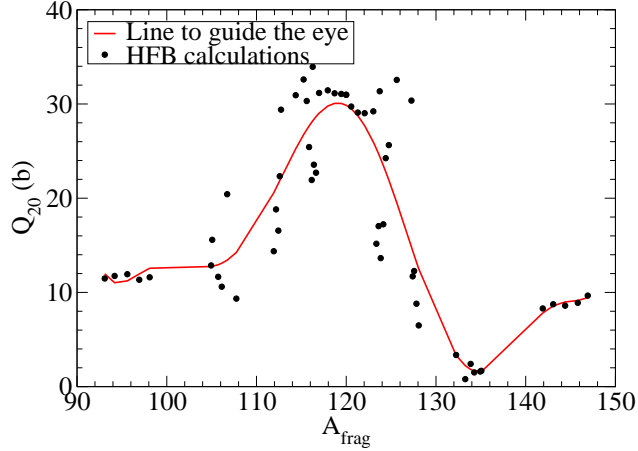


Figure 22: (Color online) Fission-fragment quadrupole moments, plotted as a function of fragment mass number, obtained from the HFB calculations immediately prior to scission in Fig. 17. A line has been drawn through the HFB results to guide the eye.

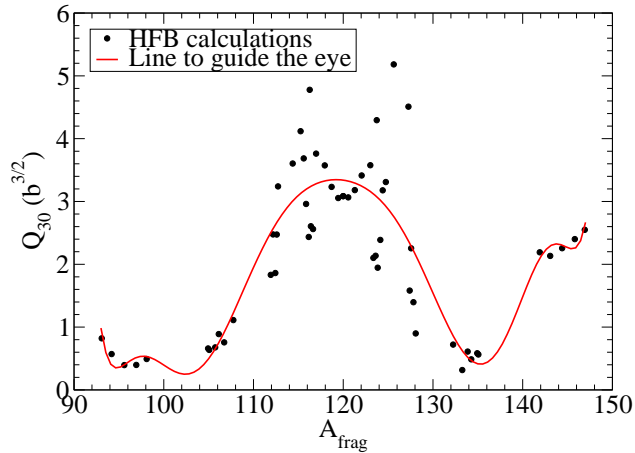


Figure 23: (Color online) Same as Fig. 22, but for the fission-fragment octupole moments.

target of ^{239}Pu . We have focused on the technical aspects of using the HFB formalism for fission studies. In particular, we have discussed some aspects of fission calculations within a one-center basis, and the importance the choice of collective coordinates in the HFB iterations for nearly-scissioned configurations. A scission line in the quadrupole-octupole plane was obtained and shows a tendency for the nucleus to reach much larger elongations in the symmetric limit before scission occurs. A similar feature was observed in the scission

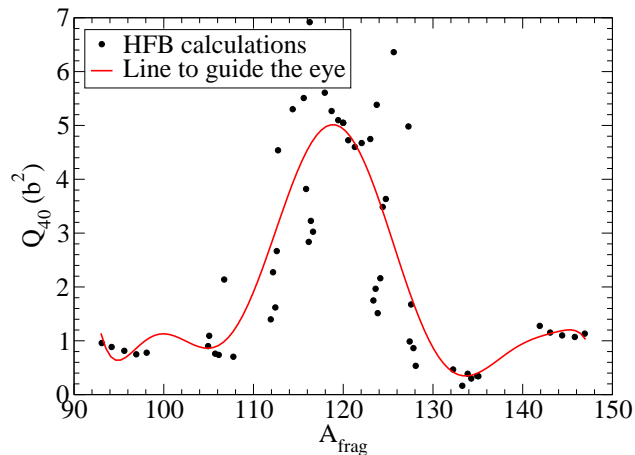


Figure 24: (Color online) Same as Fig. 22, but for the fission-fragment hexadecapole moments.

line of ^{226}Th by Dubray *et al.* [14] using two-center HFB calculations, reproduced in this work with a one-center calculation. The increased “malleability” of the nucleus near the symmetric limit is reflected in the various moments (quadrupole, octupole, hexadecapole) calculated for the fission fragments and presented here.

In a forthcoming publication, we will extract the excitation and kinetic energies of the fission fragments. We will introduce a microscopic criterion for the identification of fission fragments, and calculate their interaction energies, with special attention to the density tails discussed in this paper. Finally, the static calculations of hot fission presented here are the first step in a fully dynamical calculation of ^{240}Pu fission. Further developments are planned to explore all fission modes, from hot to cold, and to include the dynamical aspects of the theory in the calculations.

Acknowledgments

This work was performed under the auspices of the U.S. Department of Energy by the Lawrence Livermore National Laboratory under Contract DE-AC52-07NA27344.

Appendix A: MULTIPLE CONSTRAINT FORMALISM

1. Effect of the variation of a single Lagrange multiplier on the generalized density

In this appendix, we derive the formalism for solving the HFB equation with multiple constraints. The derivation generalizes the discussion in [28] to the case of multiple constraints.

In the first section, we give the essential formulas used in the adjustment of constraints. A second section illustrates the formalism with the special case of a single constraint, and the last section presents the general case of multiple constraints. Starting from the HFB equation, Eq. (9), we write for a Hamiltonian with a single constraint $\lambda\hat{F}$ introduced as is Eq. (16),

$$[\mathcal{H}(R(\lambda), \lambda), R(\lambda)] = 0$$

where

$$\begin{aligned} \langle \lambda | \hat{F} | \lambda \rangle &\equiv f(\lambda) \\ &= \frac{1}{2} \text{Tr} \hat{F} + \frac{1}{2} \text{Tr} \mathbb{F} R(\lambda) \end{aligned} \quad (\text{A1})$$

is the expectation value of \hat{F} in the corresponding HFB solution $|\lambda\rangle$, with \mathbb{F} given by Eq. (17). Consider a small variation $\delta\lambda$ of the Lagrange multiplier, leading to a new HFB solution with

$$[\mathcal{H}(R(\lambda + \delta\lambda), \lambda + \delta\lambda), R(\lambda + \delta\lambda)] = 0 \quad (\text{A2})$$

where

$$\begin{aligned} \langle \lambda + \delta\lambda | \hat{F} | \lambda + \delta\lambda \rangle &\equiv f(\lambda + \delta\lambda) \\ &= \frac{1}{2} \text{Tr} \hat{F} \\ &\quad + \frac{1}{2} \text{Tr} \mathbb{F} R(\lambda + \delta\lambda) \end{aligned} \quad (\text{A3})$$

We will now derive an explicit relation between the generalized density

$$R(\lambda) \equiv {}^{(0)}R$$

and its perturbed value, expanded to first order in $\delta\lambda$,

$$R(\lambda + \delta\lambda) \equiv {}^{(0)}R + {}^{(1)}R$$

Note that the idempotence condition in Eq. (5) implies that the matrix ${}^{(1)}R$ has the form

$${}^{(1)}\tilde{R} = \begin{pmatrix} 0 & {}^{(1)}\tilde{R}^{12} \\ {}^{(1)}\tilde{R}^{21} & 0 \end{pmatrix} \quad (\text{A4})$$

in the quasiparticle representation that diagonalizes ${}^{(0)}R$. A straightforward linearization of Eq. (A2) about ${}^{(0)}R$ gives the relation

$${}^{(1)}\vec{R} = \delta\lambda M^{-1}\vec{F} \quad (\text{A5})$$

where M is the QRPA matrix, whose elements are given by second-order derivatives of the energy with respect to the generalized density matrix [28], and where we have introduced the vector notation

$$\vec{F} = \begin{pmatrix} F^{(1,2)} \\ F^{(1,2)*} \end{pmatrix} \quad (\text{A6})$$

and similarly for ${}^{(1)}\vec{R}$. Next, from Eqs. (A1) and (A3), we deduce

$$\begin{aligned} \delta f &\equiv f(\lambda + \delta\lambda) - f(\lambda) \\ &= \frac{1}{2}\vec{F}^\dagger \cdot {}^{(1)}\vec{R} \end{aligned} \quad (\text{A7})$$

Combining this result with Eq. (A5), we can express $\delta\lambda$ in the form

$$\delta\lambda = \frac{2\delta f}{\vec{F}^\dagger \cdot (M^{-1}\vec{F})} \quad (\text{A8})$$

Equations (A5) and (A8) are the basis for the iterative procedure described in the next section that is used to solve the HFB equation under constraint.

In order to obtain a computationally efficient expression for the inverse QRPA matrix M^{-1} in Eq. (A8), we adopt the so-called ‘‘cranking’’ approximation where the residual interaction between quasiparticles is neglected in the QRPA matrix. In this case, M^{-1} takes the block-diagonal form

$$M^{-1} = \begin{pmatrix} [(\varepsilon_\mu + \varepsilon_\nu)^{-1} \delta_{\mu\sigma} \delta_{\nu\tau}] & [0] \\ [0] & [(\varepsilon_\mu + \varepsilon_\nu)^{-1} \delta_{\mu\sigma} \delta_{\nu\tau}] \end{pmatrix}$$

and therefore,

$${}^{(1)}R_{\mu\nu}^{21} = \frac{\delta\lambda}{\varepsilon_\mu + \varepsilon_\nu} \sum_{mn} (F_{mn} V_{m\mu} U_{n\nu} - F_{mn}^* U_{m\mu} V_{n\nu}) \quad (\text{A9})$$

with a corresponding expression for $\delta\lambda$.

2. Adjustment of the HFB solution in the case of one constraint

In this section, we examine in greater detail steps 7 and 8 in the description of the HFB algorithm listed in section II D. In this case, the constrained HFB equation is written

$$[\mathcal{H}(R) - \lambda\mathbb{F}, R] = 0$$

with

$$f = \frac{1}{2}\text{Tr}\hat{F} + \frac{1}{2}\text{Tr}\mathbb{F}R$$

where f is the expectation value of the constraint operator. The solution of the HFB equation then consists not only in determining R , but also the Lagrange multiplier λ that satisfies the constraint. To solve this problem, we are led to an iterative procedure wherein the Lagrange multiplier is adjusted at each iteration. Consider the n^{th} iteration, such that the generalized density matrix obtained in the previous iteration is $R^{(n-1)}$ with a corresponding Lagrange multiplier $\lambda^{(n-1)}$. The diagonalization of $\mathcal{H}(R^{(n-1)}) - \lambda^{(n-1)}\mathbb{F}$ leads to a new generalized density which we will denote $\bar{R}^{(n)}$. At this stage, the constraint is no longer necessarily satisfied and we calculate the deviation from the desired value

$$\delta f^{(n)} = f - f^{(n)}$$

We correct the Lagrange multiplier using Eq. (A8),

$$\lambda^{(n)} = \lambda^{(n-1)} + \frac{2\delta f^{(n)}}{\vec{F}^\dagger \cdot (M^{-1}\vec{F})}$$

and the generalized density using Eq. (A5),

$$R^{(n)} = \bar{R}^{(n)} + \delta\lambda M^{-1}\vec{F}$$

with

$$\delta\lambda = \lambda^{(n)} - \lambda^{(n-1)}$$

We define the n^{th} iteration with the self-consistent pair of $R^{(n)}$ and $\lambda^{(n)}$. Note that the constraint is satisfied at each iteration. This iterative process generally converges, i.e.

$$\begin{aligned} R^{(n)} &\rightarrow \bar{R}^{(n)} \rightarrow R \\ \lambda^{(n)} &\rightarrow \lambda \\ f^{(n)} &\rightarrow f \end{aligned}$$

If the difference in constraint values is very large between successive iterations (as may be the case in the first few iterations), the convergence rate can be improved by calculating the generalized density matrix at the n^{th} iteration according to

$$R^{(n)} = (1 - \alpha) \left(\bar{R}^{(n)} + \delta\lambda M^{-1} \vec{F} \right) + \alpha R^{(n-1)}$$

with the associated Lagrange multiplier

$$\lambda^{(n)} = (1 - \alpha) (\lambda^{(n-1)} + \delta\lambda) + \alpha \lambda^{(n-1)}$$

where the weight α tends to zero as the solution converges. With this prescription, the convergence of the generalized density and Lagrange multiplier are slowed down by the same amount. In other words, the desired value f for the constraint is approached in a gradual manner, so that at the n^{th} iteration

$$\left\langle \lambda^{(n)} \left| \hat{F} \right| \lambda^{(n)} \right\rangle = f^{(n)} = (1 - \alpha) f + \alpha f^{(n-1)}$$

3. Adjustment of the HFB solution in the case of multiple constraints

The results in the previous section can be readily generalized to an arbitrary number N of constraints. In this case, the HFB procedure minimizes the energy

$$\left\langle \{\lambda\} \left| H - \sum_{i=1}^N \lambda_i \hat{F}_i \right| \{\lambda\} \right\rangle$$

subject to the set of constraints

$$\left\langle \{\lambda\} \left| \hat{F}_i \right| \{\lambda\} \right\rangle = f_i, \quad i = 1, \dots, N$$

The generalized density matrix is now a function of N Lagrange multipliers, $R(\{\lambda\})$. We write

$$\begin{aligned}
R(\{\lambda + \delta\lambda\}) - R(\{\lambda\}) &\equiv {}^{(1)}R \\
&= \sum_{i=1}^N \frac{\partial R}{\partial \lambda_i} \delta\lambda_i \\
&= \sum_{i=1}^N {}^{(1)}R_i
\end{aligned} \tag{A10}$$

Clearly, ${}^{(1)}R_i$ is a variation where all the Lagrange multipliers are held fixed except for the one associated with \hat{F}_i . Therefore, ${}^{(1)}R_i$ is given by Eq. (A5) with the substitutions $\delta\lambda \rightarrow \delta\lambda_i$ and $\hat{F} \rightarrow \hat{F}_i$. In the case of multiple constraints, Eq. (A5) is therefore replaced by

$${}^{(1)}\vec{R} = \sum_{i=1}^N \delta\lambda_i M^{-1} \vec{F}_i \tag{A11}$$

Furthermore, using the generalization of Eq. (A7) to multiple constraints,

$$\begin{aligned}
\delta f_i &\equiv \left\langle \{\lambda + \delta\lambda\} \left| \hat{F}_i \right| \{\lambda + \delta\lambda\} \right\rangle - \left\langle \{\lambda\} \left| \hat{F}_i \right| \{\lambda\} \right\rangle \\
&= \frac{1}{2} \vec{F}_i^\dagger \cdot {}^{(1)}\vec{R}
\end{aligned}$$

and taking into account Eq. (A11), we finally obtain

$$\delta\lambda = T^{-1} \delta f \tag{A12}$$

where the $N \times N$ matrix T is defined by

$$T_{lm} \equiv \frac{1}{2} \vec{F}_l^\dagger \cdot (M^{-1} \vec{F}_m) \tag{A13}$$

Note that this matrix introduces correlations between all the constraints. We assume in our discussion that the inverse matrix T^{-1} exists, i.e., that the constraints are independent. Eqs. (A11) and (A12) then replace Eqs. (A5) and (A8) in the adjustment method described above.

Appendix B: TRANSLATION IN A FINITE HARMONIC OSCILLATOR BASIS

In this section, we give the explicit form for the expansion of a translated harmonic-oscillator function in a harmonic-oscillator basis. We begin with the generating function for

the Cartesian harmonic-oscillator function (Eq. (A.1) in [35]).

$$e^{-t^2+2tx/b-x^2/(2b^2)} = \sqrt{b\sqrt{\pi}} \sum_{k=0}^{\infty} \frac{2^{k/2}}{\sqrt{k!}} t^k \Phi_k(x; b) \quad (\text{B1})$$

Letting $x \rightarrow x + \Delta x$ on both sides of Eq. (B1) after some simplification, the left-hand side (LHS) can be written as

$$\begin{aligned} LHS &= \sqrt{b\sqrt{\pi}} e^{-\Delta x(x+\Delta x/2)/b^2} \\ &\times \sum_{m=0}^{\infty} \sum_{n=0}^{\infty} \frac{2^{m+n/2} (\Delta x/b)^m}{m! \sqrt{n!}} \Phi_n(x; b) t^{m+n} \end{aligned}$$

where we have used Eq. (B1) to express the LHS in terms of harmonic-oscillator functions. Equating like powers of the arbitrary variable t between the LHS and right-hand side (RHS), we obtain

$$\begin{aligned} \Phi_k(x + \Delta x; b) &= e^{-\Delta x(x+\Delta x/2)/b^2} \\ &\times \sum_{m=0}^k \frac{2^{m/2} \sqrt{k!} (\Delta x/b)^m}{m! \sqrt{(k-m)!}} \\ &\times \Phi_{k-m}(x; b) \end{aligned} \quad (\text{B2})$$

This is still a finite sum over harmonic-oscillator functions, however an overall exponential factor depending on x remains, and must be eliminated in order to obtain the expansion of $\Phi_k(x + \Delta x; b)$ on the harmonic-oscillator basis. Thus, in general, we need to derive an expansion for the expression

$$e^{2\alpha x/b^2} \Phi_i(x; b) \quad (\text{B3})$$

where $\alpha = -\Delta x/2$ and $i = k - m$ in our case. Starting from the generating function in Eq. (B1), and multiplying both sides by the exponential factor in Eq. (B3), the LHS of Eq. (B1) becomes after some simplification

$$LHS = \sqrt{b\sqrt{\pi}} e^{\alpha^2/b^2} \sum_{l=0}^{\infty} \frac{2^{l/2}}{\sqrt{l!}} e^{2\alpha t/b} \left(t + \frac{\alpha}{b}\right)^l \Phi_l(x; b)$$

Expanding in powers of the arbitrary variable t , this takes the form

$$\begin{aligned} LHS &= \sqrt{b\sqrt{\pi}} e^{\alpha^2/b^2} \sum_{l=0}^{\infty} \sum_{p=0}^{\infty} \sum_{q=0}^l \\ &\times \binom{l}{q} \frac{2^{p+l/2}}{p! \sqrt{l!}} \left(\frac{\alpha}{b}\right)^{l+p-q} \Phi_l(x; b) t^{p+q} \end{aligned}$$

Therefore, equating like powers of t between LHS and RHS, we obtain

$$e^{2\alpha x/b^2} \Phi_k(x; b) = e^{\alpha^2/b^2} \sum_{l=0}^{\infty} \sum_{q=0}^l \binom{l}{q} \frac{2^{(k+l)/2-q} \sqrt{k!}}{(k-q)! \sqrt{l!}} \times \left(\frac{\alpha}{b}\right)^{l+k-2q} \Phi_l(x; b)$$

Using this result in Eq. (B2), we obtain

$$\Phi_k(x + \Delta x; b) = e^{-\Delta x^2/(4b^2)} \times \sum_{l=0}^{\infty} C_l \left(-\frac{\Delta x}{2b}\right) \Phi_l(x; b) \quad (\text{B4})$$

where

$$C_l(\xi) = 2^{(k+l)/2} \sqrt{\frac{k!}{l!}} \xi^{(k+l)/2} \times \sum_{m=0}^k \sum_{q=0}^l \frac{(-1)^m 2^{m-q}}{m! (k-m-q)!} \binom{l}{q} \xi^{-2q}$$

Note that the expansion of the translated harmonic-oscillator function requires in principle and infinite number of terms. In practice, these translations are performed in a finite-sized basis, and the truncation of the sum in Eq. (B4) to those shells within the basis can lead to the appearance of tails for translated nuclear densities expanded in a finite harmonic-oscillator basis, as shown in Figs. 1 and 2.

-
- [1] H. Flocard, P. Quentin, D. Vautherin, and M. Veneroni, Nucl. Phys. **A231**, 176 (1974).
 - [2] J.-F. Berger, M. Girod, and D. Gogny, Nucl. Phys. **A428**, 23 (1984).
 - [3] K. Rutz, J. A. Maruhn, P. G. Reinhard, W. Greiner, Nucl. Phys. **A590**, 680 (1995).
 - [4] M. Warda, J. L. Egidio, L. M. Robledo, and K. Pomorski, Phys. Rev. C **66**, 014310 (2002).
 - [5] T. Bürnevich, M. Bender, J. A. Maruhn, P.-G. Reinhard, Phys. Rev. C **69**, 14307 (2004).
 - [6] J.-P. Delaroche, M. Girod, H. Goutte, J. Libert, Nucl. Phys. **A771**, 103 (2006).
 - [7] S. Perez-Martin and L. M. Robledo, Intl. J. Mod. Phys. **E18**, 788 (2009).
 - [8] V. Martin and L. M. Robledo, Intl. J. Mod. Phys. **E18**, 861 (2009).
 - [9] J. L. Egidio and L. M. Robledo, Phys. Rev. Lett. **85**, 1198 (2000).
 - [10] R. Smolańczuk, J. Skalski, and A. Sobiczewski, Phys. Rev. **52**, 1871 (1995).

- [11] C. R. Chinn, J.-F. Berger, D. Gogny, and M. S. Weiss, Phys. Rev. **45**, 1700 (1992).
- [12] H. Goutte, J.-F. Berger, P. Casoli, and D. Gogny, Phys. Rev. C **71**, 024316 (2005).
- [13] L. M. Robledo and W. Warda, Intl. J. of Mod. Phys. **E17**, 204 (2008).
- [14] N. Dubray, H. Goutte, and J.-P. Delaroche, Phys. Rev. C **77**, 014310 (2008).
- [15] L. Bonneau, P. Quentin, I. N. Mikhailov, Phys. Rev. C **75**, 64313 (2007).
- [16] W. Younes and D. Gogny, LLNL Tech. Rep. UCRL-TR-234682 (2007).
- [17] D. Gogny, *Proceedings of the International Conference on Nuclear Selfconsistent Fields, Trieste, 1975*, (North-Holland, Amsterdam, 1975), p. 333.
- [18] N. N. Bogoliubov, Sov. Phys. JETP **7**, 41 (1958).
- [19] D. L. Hill, and J. A. Wheeler, Phys. Rev. **89**, 1102 (1953).
- [20] J. J. Griffin, and J. A. Wheeler, Phys. Rev. **108**, 311 (1957).
- [21] Q. Haider, and D. Gogny, J. Phys. G **18**, 993 (1992).
- [22] P.-G. Reinhard, R. Y. Cusson, and K. Goeke, Nucl. Phys. **A398**, 141 (1983).
- [23] N. Onishi, R. K. Sheline, and S. Yoshida, Phys. Rev. C **2**, 1304 (1970).
- [24] P. Bonche, J. Dobaczewski, H. Flocard, P.-H. Heenen, and J. Meyer, Nucl. Phys. **A510**, 466 (1990).
- [25] M. Didong, H. Mütter, K. Goeke, and A. Faessler, Phys. Rev. C **14**, 1189 (1976).
- [26] G. Schütte, Phys. Rep. **80**, 113 (1981).
- [27] P. Ring and P. Schuck, *The Nuclear Many Body Problem* (Springer-Verlag, Berlin, 1980).
- [28] J. Dechargé and D. Gogny, Phys. Rev. C **21**, 1568 (1980).
- [29] M. Girod and B. Grammaticos, Phys. Rev. C **27**, 2317 (1983).
- [30] M. Anguiano, J. L. Egido, L. M. Robledo, Nucl. Phys. **A683**, 227 (2001).
- [31] J. L. Egido, H. J. Mang, P. Ring, Nucl. Phys. **A334**, 1 (1980).
- [32] J. L. Egido, J. Lessing, V. Martin, L. M. Robledo, Nucl. Phys. **A594**, 70 (1995).
- [33] L. M. Robledo, R. R. Rodríguez-Guzmán, P. Sarriguren, Phys. Rev. C **78**, 034314 (2008).
- [34] M. Anguiano, J. L. Egido, L. M. Robledo, Phys. Lett. **545B**, 62 (2002).
- [35] W. Younes, Comp. Phys. Commun. **180**, 1013 (2009).
- [36] L. Bonneau, Phys. Rev. C **74**, 014301 (2006).
- [37] H. Flocard, P. Quentin, A. K. Kerman, D. Vautherin, Nucl. Phys. **A203**, 433 (1973).
- [38] J. L. Egido, L. M. Robledo, R. R. Chasman, Phys. Lett. B **393**, 13 (1997).
- [39] W. Younes and D. Gogny, to be submitted to Phys. Rev. C, (2009).

- [40] B. Giraud, J. LeTourneux, and S. K. M. Wong, *Phys. Lett.* **B32**, 23 (1970).
- [41] A. Baran, A. Bulgac, M. M. Forbes, G. Hagen, W. Nazarewicz, N. Schunck, and M. V. Stoitsov, *Phys. Rev. C* **78**, 014318 (2008).
- [42] P. Möller, A. J. Sierk, and A. Iwamoto, *Phys. Rev. Lett.* **92**, 072501 (2004).
- [43] W. Younes and D. Gogny, in *Proceedings of the Fourth International Workshop on Nuclear Fission and Fission Product Spectroscopy*, Cadarache, France, 2009 (in press).
- [44] C. Wagemans, E. Allaert, A. Deruytter, R. Barthélémy, and P. Schillebeeckx, *Phys. Rev. C* **30**, 218 (1984).
- [45] A. C. Wahl, *At. Data and Nucl. Data Tables* **39**, 1 (1988).
- [46] In our original HFB calculations for ^{240}Pu , the $\langle \hat{Q}_{30} \rangle$ values for the light fragments are negative, but since the sign carries no relevant physical meaning for this quantity, we have taken its absolute value in Fig. 23.